Nature of the hemodynamic forces exerted on vascular endothelial cells or leukocytes adhering to the surface of blood vessels

Yechun Wang and P. Dimitrakopoulos[a)]
Department of Chemical and Biomolecular Engineering, University of Maryland, College Park, Maryland 20742

(Received 4 February 2006; accepted 10 July 2006; published online 29 August 2006)

The hemodynamic forces on endothelial cells or leukocytes attached to the inner surface of blood vessels affect the physiological behavior of these systems via mechano-transduction or receptor-ligand binding. The present study investigates the relative importance and nature of the two components of the hemodynamic force, i.e., the shear and normal force, on a cell and its vicinity. We consider a wide range of blood vessels (from capillaries to arteries) and cell's spreading angles. Based on computational investigation and analysis, our study demonstrates that the normal force contributes significantly to the total force on the cell; the influence is much more pronounced in small vessels. We also show that the spreading of the cell on the vessel surface should not be discounted, especially in small vessels. Our results are also applicable to the fluid forces on other protuberances of biological nature attached to vascular vessels (e.g., cancer cells and biofilm) as well as to the fluid forces over protuberances in microfluidics and porous media. © *2006 American Institute of Physics*. [DOI: 10.1063/1.2336116]

I. INTRODUCTION

Hemodynamic forces play a pivotal role in the normal and pathological behavior of vascular endothelial cells.[1–9] Hemodynamic forces exerted on leukocytes adherent to the surface of blood vessels play also a pivotal role in the cell adhesion process since they need to be balanced by the receptor-ligand binding forces on the surface of the cells.[10,11] The same is true for the fluid forces on other protuberances of biological nature in vascular vessels, such as those formed during cancer cell metastasis and biofilm formation.[12]

Several studies have considered the fluid forces on endothelial cells. Hazel and Pedley[13] studied the hemodynamic force on vascular endothelial cells in arteries by modeling the artery as a solid plane (due to its large diameter relative to the cell size), and the cell as an ellipsoidal solid protuberance. By considering various cell configurations, the study suggested that the cells respond to the flow by minimizing the total force on their nuclei. The fluid stresses on a cell adhering to a microchannel wall were studied by Gaver and Kute.[10] They considered a two-dimensional flow within two parallel plates and a semicircular hump on the lower plate to model an endothelial cell or a leukocyte adhering to the inner surface of a microvessel wall. The authors accompanied their numerical results on the fluid forces with lubrication theory for large cell sizes.

A number of authors have considered the fluid forces on leukocytes in post-capillary vessels by modeling the cells as solid spheres and the vessels as cylindrical tubes. Chapman and Cokelet determined the drag force on a single adherent leukocyte as a function of the leukocyte-to-vessel diameter ratio and the Reynolds number based on dimensionless analysis, experiments, and computations.[12,14] They showed that the drag force increases considerably in small vessels. The same authors later extended their study to multiple adherent leukocytes in post-capillary vessels.[15] They found that the drag force on a leukocyte may be greatly affected by the relative configuration of neighbor leukocytes. Similar results were reported by Sugihara-Seki and Skalak.[16,17] In a later study, Sugihara-Seki showed that for moderate and small vessels (with respect to the cell size), the flow around an adherent leukocyte in a cylindrical vessel cannot be approximated by that in a parallel-plate channel.[18] Sugihara-Seki and Schmid-Schönbein determined the shear stress distribution on the leukocyte and its vicinity for adherent, rolling, and free-suspended leukocytes.[19]

In the studies mentioned above, the surrounding liquid was modeled as a Newtonian fluid. Das, Johnson, and Popel determined the flow resistance due to leukocyte adhesion by modeling the surrounding liquid as a non-Newtonian Casson fluid except very close to the vessel wall.[20] Based on that study, the increase of vascular resistance due to the leukocyte adhesion is smaller for a non-Newtonian fluid than that for a Newtonian fluid, but the difference is rather small. Liu and Wang accounted for the cell's interfacial deformation by considering three possible models (a single drop, a compound drop, and a nucleus drop) for a two-dimensional adherent leukocyte in steady shear flow.[21] Models to describe the receptor-ligand bonds for cell adhesion have also been employed, e.g., Refs. 11 and 22.

Our interest in these physical systems focuses on determining the nature of the hemodynamic force on these cells as well as the relative importance of the two components of the hemodynamic force, i.e., the shear stress and the normal force. We emphasize that a plethora of studies, mainly in the past two decades, have attributed the behavior, or changes in the behavior, of the endothelium to one of the two compo-

[a)]Electronic mail: dimitrak@eng.umd.edu

nents of the hemodynamic force, i.e., the effects of the shear stress.

For example, the shear stress was found to affect the production of prostacyclin and nitric oxide,[1,2] the endothelial hydraulic conductivity through signal transduction,[3] and the regulation of occludin content and phosphorylation.[4] The ability of endothelial cells to induce adhesion and migration of flowing neutrophils was found to be affected by the magnitude of shear stress in the presence of tumor necrosis factor-a;[5] this ability was also found to be affected by oscillatory shear stress.[6] The endothelial surface layer (glycocalyx) may act as a mechano-transducer of the fluid shear stress to the actin cortical cytoskeleton of the endothelial cells.[7] The biomechanical forces also affect the endothelial structure and functions such as the permeability to macromolecules, lipoprotein accumulation, and repair near branch points.[8] In addition, shear stress acting at the endothelium surface was found to produce rapid deformation of intermediate filament networks.[9] Thus, the influence of the second component of the hydrodynamic force on the endothelium, i.e., the normal force or pressure, has been overlooked.

In our recent Letter,[23] based on computational investigation and scaling analysis, we demonstrated that the normal force contributes significantly to the hemodynamic force on the endothelial cells, especially for small vessels. Therefore, our study suggested that the behavior of the endothelium in arteries, veins, and especially in arterioles, venules, and capillaries is also affected by the normal force exerted on it. The significant contribution of the normal force on the vascular endothelium was also shown by King,[24] who considered high Reynolds number flows in a two-dimensional microchannel used for cell detachment, and employed potential flow analysis. We note that King's analysis is restricted to two-dimensional geometries and high Reynolds number flows, and thus it is applicable to flows in large vessels (i.e., arteries and veins). On the other hand, our previous investigation[23] is valid for three-dimensional geometries and covers both large and small vessels, i.e., from arteries down to capillaries. In our previous study,[23] our interest was concentrated on the hemodynamic force and its component over the entire endothelial cell (i.e., we did not consider these forces locally on the cell's surface).

In the present paper, we extend our previous study[23] in several ways. First, we investigate the hemodynamic force and its components (i.e., shear stress and normal force) both over the entire endothelial cell and locally on the cell's surface. The interest in such a study is motivated by the ambiguity in the associated mechanism of mechano-transduction (i.e., do the cells convert their total or local force into biochemical signals?). Our results show that even locally the contribution of the normal force (or pressure) is significant and thus the effects of the normal force cannot be discounted. Second, we improve our physical understanding on the nature of the fluid force components by utilizing the predictions of the scaling analysis presented in our previous paper,[23] which is quantitatively valid only for very large vessels and very spread cells. In the current study, by employing numerical results, we show that the predictions of the scaling analysis (and thus the associated physical understanding) are qualitatively valid for a wide range of vessels and spreading angles. Outside this range, our numerical investigation also explains the nature of the components of the hemodynamic force on the cells. Third, we also consider much less spread cells (or very large spreading angles); physically these cells may represent leukocytes (white blood cells), cancer cells, or biofilm adhering to the inner surface of vascular vessels. Our study suggests that the effects of the normal force component are much more pronounced for these less spread cells; this conclusion directly affects the cell adhesion and thus the progress of associated diseases.

In the case of much less spread cells adhering in small vessels (i.e., to the limit of simple touch), the relative importance of the normal force component to the total hemodynamic force on the cells was discussed by Sugihara-Seki.[17,18] Our study extends the aforementioned ones in that we consider the entire range of spreading angles and vascular vessels, and most importantly we identify the nature of the normal and shear force components on the adherent cells.

In this study, we consider Stokes flow of a Newtonian fluid around a solid spherical-like cell in a cylindrical vessel and investigate the shear stress and normal force over the cell and its vicinity as the spreading of the cell and its size (relatively to the vessel radius) change. For small and moderate spreading angles, our modeling represents vascular endothelial cells while large spreading angles better represent adherent leukocytes. In the former case, the hump represents the nucleus of the endothelial cell protruding above the rest of the cellular surface.[13] Since the cell size is a few micrometers, i.e., $O(\mu\text{m})$, if we consider flow in capillaries (with a typical diameter of 8 μm) as well as in arterioles and venules (with a typical diameter of 10–140 μm),[25] we have to explicitly consider the curvature of the vessel wall. By considering a wide range of cell sizes (relatively to the vessel diameter), from very small values up to $O(1)$, our results are applicable to flows in both large and small vessels, i.e., from arteries and veins down to small capillaries. In the case of adherent leukocytes with a typical diameter of 8 μm, our modeling applies to the case of adherent leukocytes in postcapillary or larger vessels.

In these systems, due to the small size of the cell (and possibly that of the vessel), the Reynolds number of the flow near the cell is small and thus the assumption of Stokes flow is well justified.[25,26] [For example, for flow in large arteries with a diameter of 15 mm and average Reynolds number 500,[25] the characteristic Reynolds number for a protuberance of an $O(\mu\text{m})$ size is smaller than 1; this Reynolds number is much smaller than 1 for flows in arterioles, venules, and capillaries.] Our interest in the cell spreading results from the fact that both endothelial cells and leukocytes may spread into different configurations on a vessel, as recent experimental findings suggest.[27] The assumption of the Newtonian surrounding fluid in large vessels is rather well justified based on the results of Das, Johnson, and Popel.[20] For small vessels (e.g., capillaries), our present study does not take into account the flowing blood particles such as red and white cells. These particles induce a higher flow blocking and are expected to increase the normal force contribution to the hemodynamic force on the endothelial cells and adherent leu-

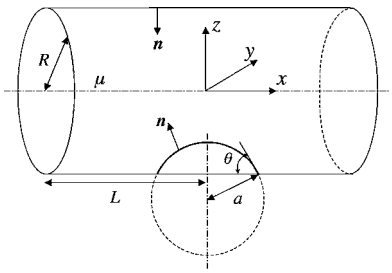

FIG. 1. A cell attached to the inner surface of a blood vessel.

kocytes (e.g., see Ref. 28); thus the consideration of these particles is expected to reinforce the major physical conclusions of the current study. We emphasize that in the case of endothelial cells, the intercell influence is weak due to the fast decay of the perturbation force on the cell and the large intercell distance with respect to the cell size;[13] thus our investigation of an isolated endothelial cell is well justified. Similarly, in the case of less spread cells, our investigation also represents the case of multiple adherent cells assuming that these cells are not very close together. (Based on experimental findings, the intercell influence is negligible if the distance of adherent leukocytes is only a few times their size;[12] this is also supported by our numerical results for the distribution of the shear stress and the normal force in the vicinity of the cell shown in Figs. 8, 10, 13, and 14.) Therefore, in both physiological systems of interest, i.e., endothelial cells and leukocytes adhering to blood vessels, our simplified model is able to capture the important physics of the complicated realistic problem.

In the current paper, we focus our attention on protuberances of biological nature in vascular vessels such as endothelial cells, adherent leukocytes, and cancer cells.[12] However, our study also helps to explain the nature of fluid forces over protuberances in microfluidics and porous media, e.g., the ones formed by the adhesion of capsules and cells in microfluidic devices, and the biofilm formation.

II. MATHEMATICAL FORMULATION

We consider a three-dimensional cell attached to the inner surface of a vessel as illustrated in Fig. 1. The vessel is modeled as a cylindrical tube with radius R and half-length L. The cell is modeled as a spherical cap with radius a. The cell size is specified by its volume V or equivalently by the radius $\tilde{a}$ of a spherical cell with identical volume, i.e.,

$$\tilde{a} = \left(\frac{3V}{4\pi}\right)^{1/3}. \tag{1}$$

The undisturbed flow far from the cell is a Poiseuille flow, $\boldsymbol{u}^{\infty} = U(1-(y^2+z^2)/R^2, 0, 0)$, where U is the (maximum) velocity at the centerline.

For a given cell volume V and vessel radius R, the spreading of the cell on the vessel surface is controlled by the angle θ defined in Fig. 1. Due to the vessel's cylindrical shape, the spreading angle θ along the contact line (i.e., the intersection of the cell surface with the vessel surface) is a function of the azimuthal angle ϕ as shown in Fig. 2. For a

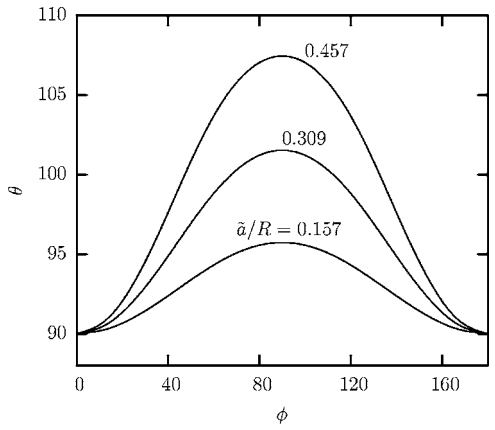

FIG. 2. The variation of the spreading angle θ as a function of the azimuthal angle ϕ for $\theta_0 = 90°$ and different cell sizes $\tilde{a}/R$. For this θ_0, the depicted values of $\tilde{a}/R$ correspond to $a/R = 0.2, 0.4, 0.6$.

given size $\tilde{a}/R$ of a spherical-like cell, the relationship between the spreading angle θ and the azimuthal angle ϕ may be determined by the spreading angle θ_0 at $\phi = 0°$. In this study, the angle θ_0 is employed to define the spreading of the cell on the vessel surface. We cover a wide range of spreading considering cells with $\theta_0 = 5°, 10°, 20°, \ldots, 160°$ (increments of 10°). The small and moderate angles better represent vascular endothelial cells as shown in Fig. 3(a) while for large spreading angles our modeling represents adherent leukocytes as seen in Fig. 3(b).

Due to the small size of the cell (and possibly that of the vessel), the flow near the cell occurs at low Reynolds numbers. Thus the governing equations are the Stokes equation along with continuity,

$$\nabla \cdot \boldsymbol{\sigma} \equiv -\nabla p + \mu \nabla^2 \boldsymbol{u} = 0 \quad \text{and} \quad \nabla \cdot \boldsymbol{u} = 0, \tag{2}$$

where $\boldsymbol{\sigma}$ is the stress tensor, p is the dynamic pressure, μ is the viscosity of the fluid, and $\boldsymbol{u}$ is the velocity vector.

The fundamental solution for the three-dimensional Stokes equations is designated S_{ij} and the associated stress is T_{ijk}. These solutions may be written in the form

$$S_{ij} = \frac{\delta_{ij}}{r} + \frac{\hat{x}_i \hat{x}_j}{r^3} \quad \text{and} \quad T_{ijk} = -6\frac{\hat{x}_i \hat{x}_j \hat{x}_k}{r^5}, \tag{3}$$

where $\hat{\boldsymbol{x}} = \boldsymbol{x} - \boldsymbol{x}_0$ and $r = |\hat{\boldsymbol{x}}|$.

By introducing the fundamental solution and integrating over a volume of fluid bounded by a surface S, the velocity at a point $\boldsymbol{x}_0$ on the surface S is expressed by the following boundary integral equation:

$$\boldsymbol{u}(\boldsymbol{x}_0) = -\frac{1}{4\pi\mu}\int_S [\boldsymbol{S}(\hat{\boldsymbol{x}}) \cdot \boldsymbol{f}(\boldsymbol{x}) - \mu \boldsymbol{T}(\hat{\boldsymbol{x}}) \cdot \boldsymbol{u}(\boldsymbol{x}) \cdot \boldsymbol{n}(\boldsymbol{x})] dS. \tag{4}$$

This equation relates the velocity $\boldsymbol{u}$ at each point $\boldsymbol{x}_0$ on the boundary S as a surface integral of the force vector $\boldsymbol{f} = \boldsymbol{\sigma} \cdot \boldsymbol{n}$ and the velocity $\boldsymbol{u}$ over all points $\boldsymbol{x}$ on the same boundary. The unit normal vector $\boldsymbol{n}$ points into the domain volume surrounded by the boundary S as shown in Fig. 1. A detailed derivation may be found in Pozrikidis.[29] The main benefit of the transformation from the partial differential equations (2)

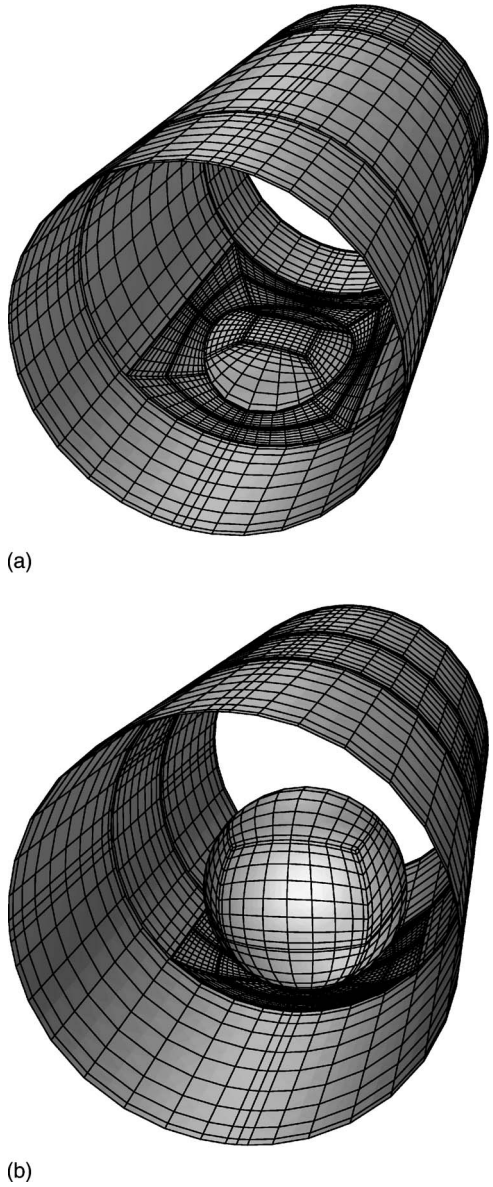

FIG. 3. Three-dimensional view of a cell adhering to the surface of a blood vessel. (a) An endothelial cell with $\theta_0=30°$. (b) A leukocyte with $\theta_0=160°$.

to the boundary integral equation (4) is the great reduction in computational time since a fully three-dimensional problem can be described and solved using only two (curvilinear) coordinates.

For the current problem, the surface S consists of the solid surface S_s of the cell and the vessel wetted by the surrounding fluid as well as by the fluid surface S_f of the vessel's inlet and outlet far away from the cell. The relevant boundary conditions are

$$\boldsymbol{u}=0 \quad \text{on the solid boundary } S_s, \tag{5}$$

$$\boldsymbol{u}=\boldsymbol{u}^{\infty} \text{ or } \boldsymbol{f}=\boldsymbol{f}^{\infty} \quad \text{on the fluid boundary } S_f, \tag{6}$$

where $\boldsymbol{f}^{\infty}$ is the force associated with the undisturbed Poiseuille flow $\boldsymbol{u}^{\infty}$ far from the cell.

The numerical solution of the boundary integral equation, Eq. (4), is achieved through the spectral boundary element method.[30,31] Briefly, each boundary is divided into a moderate number of surface elements that are parametrized by two variables ξ and η on the square interval $[-1,1]^2$. The geometry and physical variables are discretized using Lagrangian interpolation in terms of these parametric variables. The base points (ξ_i,η_i) for the interpolation are chosen as the zeros of orthogonal polynomials of Gauss-type. This is equivalent to an orthogonal polynomial expansion and yields the spectral convergence associated with such expansions. The discretizations are substituted into the appropriate boundary integrals and the quadratures are evaluated using adaptive Gaussian quadrature. Further details are given in the aforementioned references.[30,31]

The boundary integral equation (4) admits two different types of points. The collocation points $\boldsymbol{x}_0$, where the equation is required to hold, and the basis points $\boldsymbol{x}$, where the physical variables $\boldsymbol{u}$ and $\boldsymbol{f}$ are specified or determined. The spectral boundary element method as implemented here employs collocation points $\boldsymbol{x}_0$ of Legendre–Gauss quadrature, i.e., in the interior of the elements. As a result, the boundary integral equation holds even for singular elements, i.e., the elements that contain the contact line where the normal vector is not uniquely defined. In addition, we use basis points $\boldsymbol{x}$ of Legendre–Gauss–Lobatto quadrature (see Secs. 2.2.3 and 2.3 in Ref. 32), and thus the physical variables are determined in the interior and on the edges of the spectral elements. The discretized system of equations is solved using a Gauss elimination algorithm from the LAPACK software library.

Three-dimensional views of the problem geometry are illustrated in Fig. 4. In the present paper, the majority of computations were performed with a discretization employing $N_E=39$ elements. The surface of the cell, by being projected onto a cube, is divided into a total of five elements as shown in Figs. 4(a) and 4(c). (For cells with spreading angle $\theta_0>90°$, nine elements were also employed for the cell geometry.) As shown later in Sec. IV, the immediate vicinity of the cell on the vessel surface experiences a rapid change in the shear stress and the normal force. To achieve a sufficient accuracy in this area, two rows with eight elements each are employed as shown in Fig. 4(c). The vessel surface above the cell is usually discretized into two spectral elements. (Additional elements were used for large enough cells.) The remaining cylindrical surface is divided into three rows with at least two elements each; the length of each row increases progressively with the distance from the cell surface, as seen in Figs. 4(a) and 4(c). Finally the vessel's inlet and outlet are discretized into two elements each, as shown in Fig. 4(b). We note that the specific element distribution produces a sufficient accuracy even in the most challenging cases; on the other hand, in most cases a sufficient accuracy may also be achieved even with a smaller number of spectral elements N_E.

To determine a sufficient number of basis points N_B on each element, several convergence tests were performed for different cell sizes $\tilde{a}/R$ and spreading angles θ_0, by increasing the number of basis points N_B from 5 to 15. In all cases, the results show an exponential convergence associated with the spectral discretization, as seen in Fig. 5 for a typical test problem. In this paper, we have employed $N_B=11$ or 13 basis

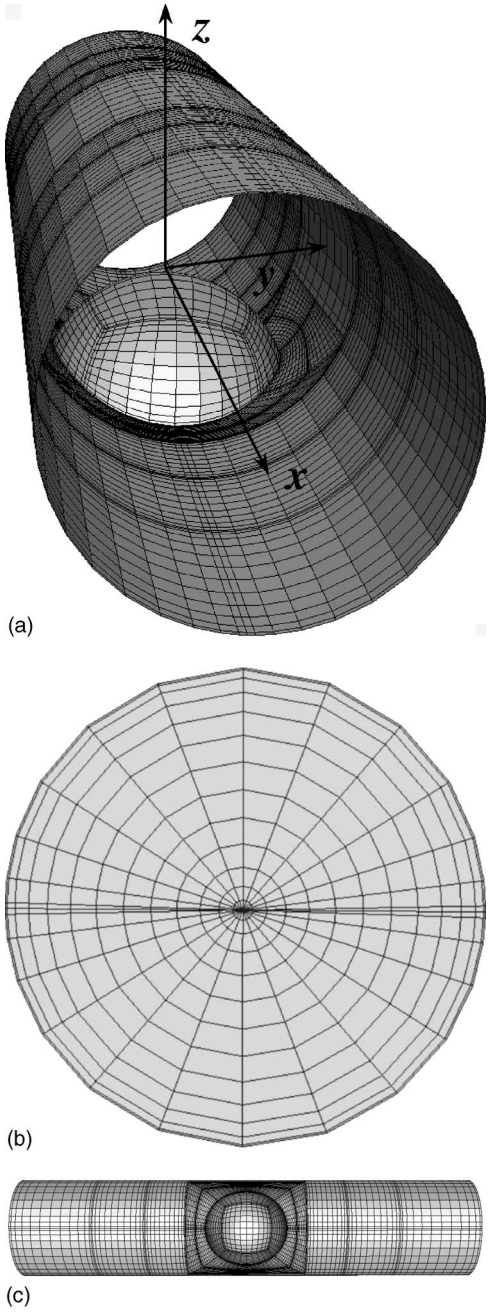

FIG. 4. Discretization of geometry for spectral boundary element calculations: (a) solid surface of cell and vessel, (b) fluid surface of vessel's inlet or outlet, (c) bottom view of the entire geometry. Each figure illustrates Lobatto distribution of nodal lines for the corresponding geometry.

points that are sufficient to produce a negligible error even in the most challenging cases.

The problem studied in this paper admits two levels of symmetry about the planes $y=0$ and $x=0$. Exploiting these symmetries reduces the memory requirements by a factor of 4^2, the computational time for the system matrices by a factor of 4, and the solution time for the linear systems by a factor of 4^3. All computations were performed on Linux PC workstations and on the shared-memory supercomputer IBM pSeries 690 provided by the National Center for Supercomputing Applications (NCSA) in Illinois.

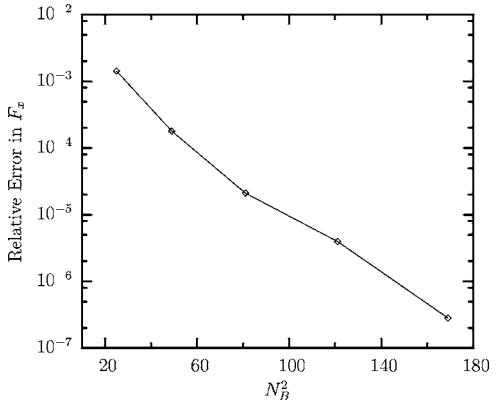

FIG. 5. Relative error in the computed total force F_x on the cell for a typical problem with $\tilde{a}/R=0.384$ (i.e., $a/R=0.5$) and $\theta_0=90°$, as the number of basis points N_B increases from 5 to 13. (The results for $N_B=15$ were used for the error determination.) This figure was generated by employing $N_E=39$ spectral elements; the resulting exponential convergence is mainly associated with the spectral discretization on the cell and thus it can also be achieved with a smaller number of spectral elements on the vessel wall.

III. DEFINITION OF PHYSICAL VARIABLES

In this paper, we study the (local) shear stress magnitude τ and normal force f_n on the surface of the cell and its vicinity defined by

$$\tau=\sqrt{(f_x^L)^2+(f_y^L)^2} \quad \text{and } f_n=f_z^L, \tag{7}$$

respectively. In addition, we study the total force F_x and the torque T_y on the cell defined by

$$F_x=\int_{S_c} f_x\,dS \quad \text{and } T_y=\int_{S_c}(\boldsymbol{l}\times\boldsymbol{f})_y\,dS, \tag{8}$$

where S_c is the cell's surface area. In these equations, $\boldsymbol{f}$ is the force vector defined at the global Cartesian coordinate system while $\boldsymbol{f}^L=(f_x^L,f_y^L,f_z^L)$ is the same vector defined at a local Cartesian coordinate system at each surface point with the x^L and y^L axes in the tangent plane and the z^L axis parallel to the normal vector $\boldsymbol{n}$. The vector $\boldsymbol{l}$ denotes the distance from the cell surface to the attachment center of the cell on the vessel wall. Due to symmetry, the remaining components of the total force and torque, i.e., F_y, F_z, T_x, and T_z, are identically zero.

The vessel radius R is used as the length scale and the maximum undisturbed velocity U as the velocity scale. As the scale for the shear stress τ and normal force f_n, we use the shear stress on the vessel wall far from the cell, $\tau_{\text{wall}}^{\infty}=2\mu U/R$. (The ratio $\tau/\tau_{\text{wall}}^{\infty}$ demonstrates the amplification in the shear stress caused by the presence of the cell.) From Eq. (8), $F_x\sim R^2\boldsymbol{f}\sim R^2\tau_{\text{wall}}^{\infty}$ while $T_y\sim R^3\boldsymbol{f}\sim R^3\tau_{\text{wall}}^{\infty}$. Therefore, in this paper we choose $R^2\tau_{\text{wall}}^{\infty}$ and $R^3\tau_{\text{wall}}^{\infty}$ as the scales for the total force and torque, respectively.

In this study, we assume that the flow rate Q inside the vessel is fixed, i.e., $Q=\pi R^2U/2$. We prefer to define the problem via a fixed flow rate instead of specifying the pressure drop Δp at the edges of the vessel since in the latter case the problem behavior, if scaled with the flow rate, becomes independent of the pressure drop Δp (as also shown in Ref. 10 for the two-dimensional analog of the current problem).

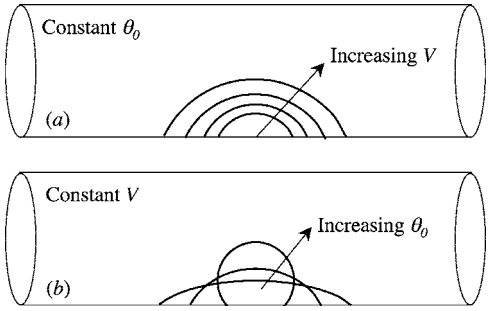

FIG. 6. Illustration of the variation of the two independent geometric parameters of the current problem. (a) Increase in the cell volume V (or length $\tilde{a}$) for a given vessel radius R while the spreading angle θ_0 remains constant. (b) Increase in the angle θ_0 with constant cell volume and vessel radius.

For a given flow rate Q, the problem of determining the force field on the cell and its vicinity depends on two independent geometric parameters: the size of the cell with respect to the vessel radius, $\tilde{a}/R$, and the spreading angle θ_0. In this study, we have chosen to define the cell size (or volume) through the characteristic length $\tilde{a}$ defined by Eq. (1) instead of the radius a of the spherical cell (shown in Fig. 1) because in the latter case a change in the cell radius a (for a given vessel radius R) may result from a change in the cell volume and/or the spreading angle θ_0. (Note that for a given cell volume V, the two dimensionless parameters of the current problem, i.e., $\tilde{a}/R$ and θ_0, are independent.)

Thus in Sec. IV we present the influence of two parameters, $\tilde{a}/R$ and θ_0, on the force field on the cell and its vicinity. As shown in Fig. 6(a), for a given vessel radius R and spreading angle θ_0, by increasing the size of the cell $\tilde{a}$, the surface area of the cell along with its height and its frontal area increase, which results in a larger blocking in the flow. An equivalent physical problem is to decrease the radius of the vessel R for a fixed cell volume (or $\tilde{a}$) and spreading angle θ_0. Therefore, our results provide insight into the blocking of the endothelial cells and leukocytes as the size of the vessel decreases. On the other hand, for a given cell volume and vessel radius, by increasing the spreading angle θ_0, the cell's height and the blocking of the cell on the flow also increase, as seen in Fig. 6(b). Therefore, by increasing $\tilde{a}/R$ or θ_0, an increase in the force on the cell is expected, as discussed in Sec. IV.

IV. RESULTS

We begin our investigation by considering the (local) shear stress vector $\boldsymbol{\tau}=(f_x^L, f_y^L, 0)$ over the cell and its vicinity shown in Fig. 7 for a rather large cell with a radius half the vessel radius (or $\tilde{a}/R=0.384$) and spreading angle $\theta_0=90°$. This figure is a three-dimensional quiver plot where the arrows start from the geometry surface and their length is proportional to the magnitude of the shear stress. As the fluid flows past the cell, the shear stress increases with the height of the surface with a maximum at the peak of the cell due to symmetry. From this figure, it is also evident that at the lower part of the cell and its nearby area on the vessel the shear stress diminishes.

To investigate further the distribution of the shear stress over the cell, in Fig. 8 we plot the magnitude of the shear stress $\tau=\sqrt{(f_x^L)^2+(f_y^L)^2}$ as a function of the arc length s_{xz} (measured from the cell peak) along the cross section of the geometry surface with the plane $y=0$ for the same spreading angle as before, i.e., $\theta_0=90°$, and for different cell sizes $\tilde{a}/R$. This figure clearly shows that the shear stress distribution has been greatly influenced by the presence of the cell due to the associated flow blocking. The stress on the upper part of the cell is much larger than that on the vessel far from the cell, $\tau_{\text{wall}}^{\infty}$, with a maximum at the cell peak due to symmetry. On the other hand, the shear stress diminishes on the lower part of the cell and its neighbor area on the vessel wall, and even approaches zero near the contact line. Therefore, this behavior is similar to that found in the case of two- and three-dimensional protuberances on solid planes, e.g., Refs. 10 and 33–35.

Figure 8 also shows the influence of the cell size $\tilde{a}/R$ on

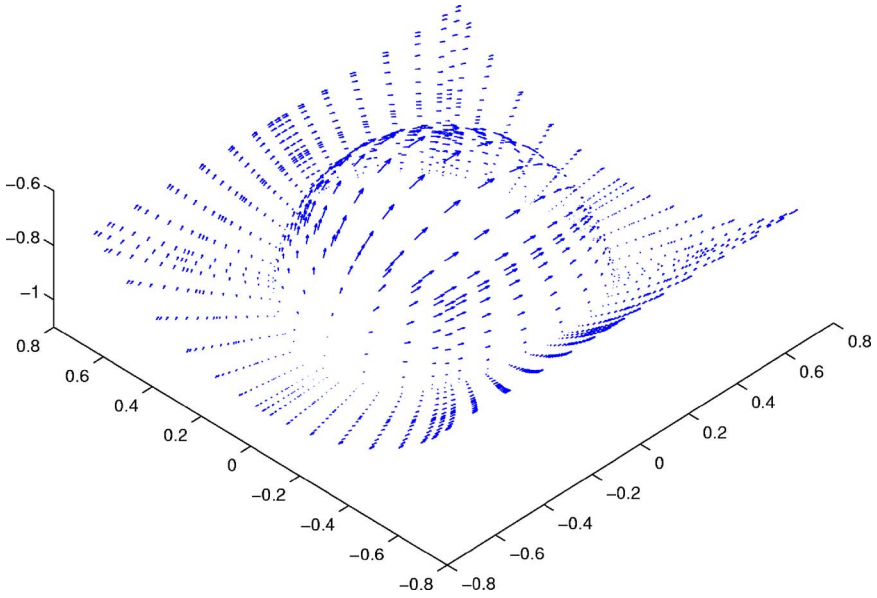

FIG. 7. A three-dimensional quiver plot for the shear stress vector $\boldsymbol{\tau}=(f_x^L, f_y^L, 0)$ for a cell with $\tilde{a}/R=0.384$ and $\theta_0=90°$. (For this spreading angle, the cell size corresponds to $a/R=0.5$, i.e., a spherical-like cell with radius half the vessel radius.)

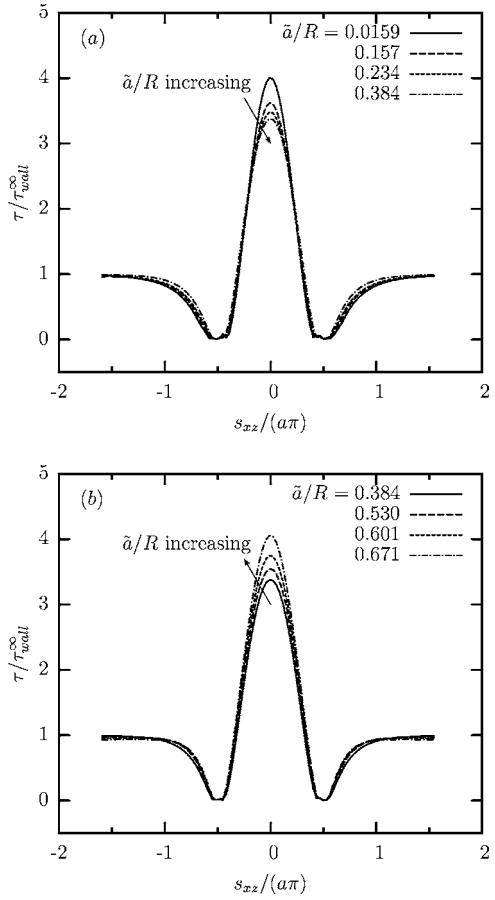

FIG. 8. Influence of the cell size $\tilde{a}/R$ on the shear stress. (a) Variation of the shear stress magnitude τ as a function of the arc length s_{xz} (measured from the cell peak) along the cross section of the geometry surface with the plane $y=0$ for spreading angle $\theta_0=90°$. The depicted values of $\tilde{a}/R$ correspond to $a/R=0.02,0.2,0.3,0.5$. (b) As in (a) but for values of $\tilde{a}/R$ corresponding to $a/R=0.5,0.7,0.8,0.9$.

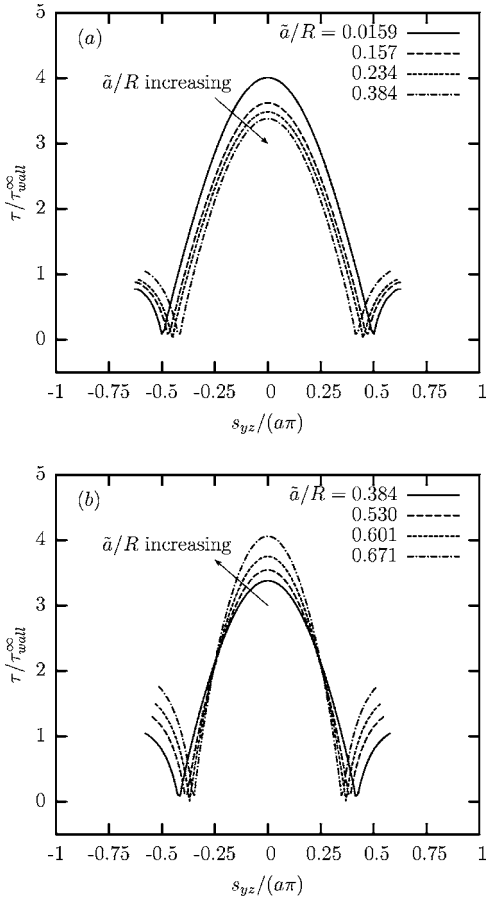

FIG. 9. Influence of the cell size $\tilde{a}/R$ on the shear stress. (a) Variation of the shear stress magnitude τ as a function of the arc length s_{yz} (measured from the cell peak) along the cross section of the geometry surface with the plane $x=0$ for spreading angle $\theta_0=90°$. The depicted values of $\tilde{a}/R$ correspond to $a/R=0.02,0.2,0.3,0.5$. (b) As in (a) but for values of $\tilde{a}/R$ corresponding to $a/R=0.5,0.7,0.8,0.9$.

the shear stress distribution. In particular, by increasing the cell size from small values, the magnitude τ of the shear stress on the top of the cell (along with its maximum value) decreases until $\tilde{a}/R \approx 0.384$. Further increase in the cell size $\tilde{a}/R$ results in an increase in the shear stress. The same behavior is also shown in Fig. 9, where we plot the variation of the shear stress magnitude along the cross section of the geometry surface with the plane $x=0$ for the same set of parameters as in Fig. 8.

The influence of the spreading angle θ_0 on the shear stress distribution is shown in Fig. 10, where we plot the shear stress magnitude τ along the cross section of the geometry surface with the planes $y=0$ and $x=0$ for a typical cell size $\tilde{a}/R$. This figure reveals that on the upper part of the cell, the shear stress magnitude shows a monotonic increase with the spreading angle, as expected since in this case the height and the frontal area of the cell increase and thus the cell provides a higher blocking to the vessel flow [see also Fig. 6(b) in Sec. III].

It is of interest to note that for small angles θ_0, the shear stress magnitude τ along the plane $y=0$, after approaching zero near the contact line, shows a rapid transition on the vessel surface near the cell, in distinct contrast to its variation for large angles as shown in Fig. 10(a). This difference is associated with the richness of possible behaviors of three-dimensional flows around protuberances including stagnation and spiral points. Since further analysis on this issue is beyond the scope of the present study, the interested reader is referred to relevant publications, e.g., Refs. 35 and 36.

The comprehensive plot shown in Fig. 11 demonstrates the influence of both the cell size $\tilde{a}/R$ and spreading angle θ_0 on the maximum shear stress magnitude $\tau^{\max}$. Several conclusions can be drawn from this figure. For small angles, the maximum shear stress is independent of the cell size $\tilde{a}/R$ as the curves for $\theta_0=5°-40°$ reveal. On the other hand, for large angles the maximum shear stress shows a weak increase when the cell size $\tilde{a}/R$ decreases from small values and a large increase when the cell size increases from large values. The minimum $\tau^{\max}$ occurs near $\tilde{a}/R=0.384$. The strong dependence of $\tau^{\max}$ on the cell size is much more pronounced at large angles as the curves for $\theta_0=100°-160°$ reveal. In addition, for a specific cell size $\tilde{a}/R$, the maximum shear stress magnitude $\tau^{\max}$ increases monotonically with the spreading angle θ_0; the increase is much more pronounced at large cell sizes.

We now turn our attention to the (local) normal force on

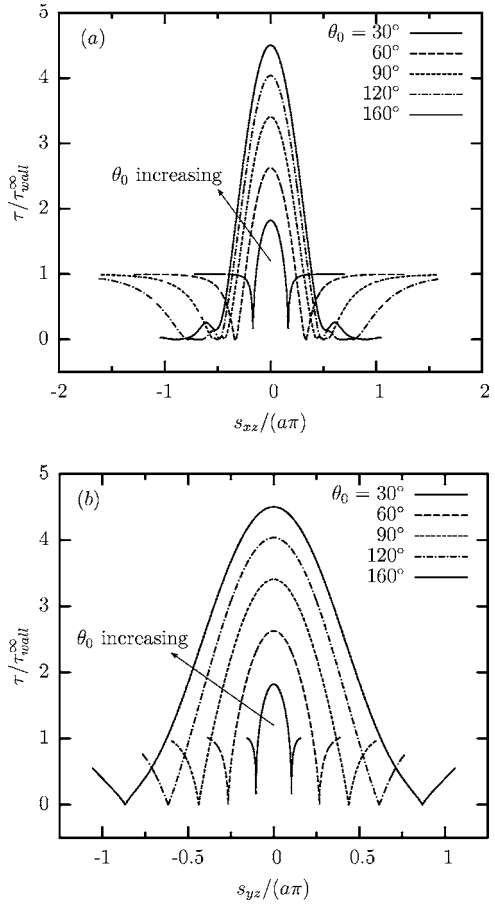

FIG. 10. Influence of the spreading angle θ_0 on the shear stress. (a) Variation of the shear stress magnitude τ as a function of the arc length s_{xz} (measured from the cell peak) along the cross section of the geometry surface with the plane $y=0$ for a cell with $\tilde{a}/R=0.30$ and for $\theta_0=30°, 60°, 90°, 120°, 160°$. (b) As in (a) but for the plane $x=0$.

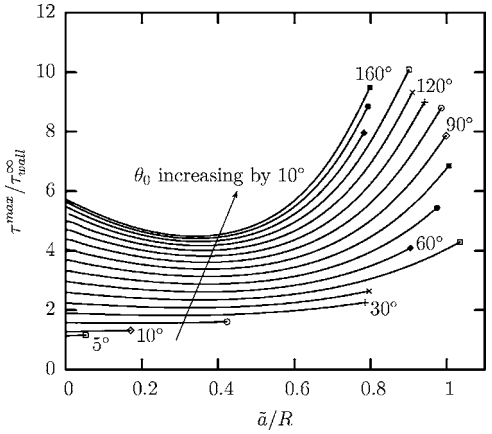

FIG. 11. Maximum magnitude of the shear stress $\tau^{\max}$ versus the cell size $\tilde{a}/R$. The spreading angle θ_0 varies from 5° to 160°.

the cell and its vicinity. Figure 12 shows a three-dimensional quiver plot of the normal force vector $\boldsymbol{f}_n=(0,0,f_z^L)$ for a cell with $\tilde{a}/R=0.384$ and $\theta_0=90°$. At the upstream portion of the cell and its vicinity, the normal force points toward the geometry surface (i.e., in the opposite direction with respect to the normal vector $\boldsymbol{n}$) while the opposite happens at the downstream portion of the cell. In addition, the normal force is higher near the intersection of the cell with the vessel while it decreases as we move toward the plane $y=0$.

The distribution of the normal force on the cell and its vicinity is shown in Fig. 13, where we plot the normal force $f_n=f_z^L$ along the cross section of the geometry surface with the plane $y=0$ for a cell with spreading angle $\theta_0=90°$ and for different sizes $\tilde{a}/R$. Clearly the presence of the cell results in a significant modification of the normal force (or pressure) over the cell and its vicinity. We emphasize that the normal force is the opposite of the pressure, i.e., $p=-f_n$ and thus the pressure is higher at the upstream portion of the cell and lower at its downstream portion. By increasing the cell size, the upstream and downstream change in the normal force (with respect to its value in the absence of the cell) increases monotonically, in distinct contrast to the behavior of the magnitude of the shear stress shown in Fig. 8. (We emphasize that the undisturbed normal force, i.e., in the absence of the cell, shows a linear variation with position that matches that in the presence of the cell shown in Fig. 13 far from the cell's location.)

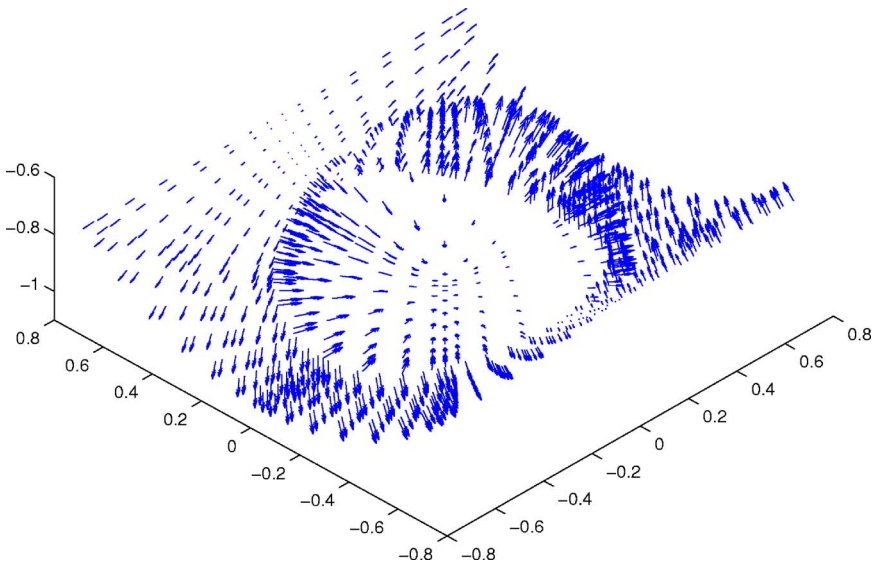

FIG. 12. A three-dimensional quiver plot of the normal force $\boldsymbol{f}_n=(0,0,f_z^L)$ for a cell with $\tilde{a}/R=0.384$ and $\theta_0=90°$. (For this spreading angle, the cell size corresponds to $a/R=0.5$, i.e., a spherical-like cell with radius half the vessel radius.) The arrows start from the geometry surface while their length is proportional to the magnitude of the normal force.

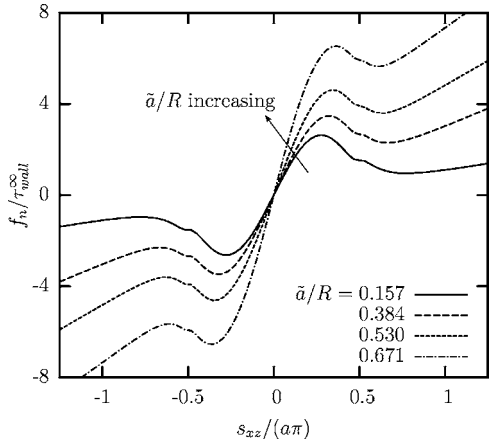

FIG. 13. Influence of the cell size $\tilde{a}/R$ on the normal force: variation of the normal force f_n as a function of the arc length s_{xz} (measured from the cell peak) along the cross section of the geometry surface with the plane $y=0$ for spreading angle $\theta_0=90^\circ$. The depicted values of $\tilde{a}/R$ correspond to $a/R=0.2,0.5,0.7,0.9$. Note that the normal force is the opposite of the pressure, i.e., $p=-f_n$ while the reference pressure $p_0=0$ is taken at the peak of the cell.

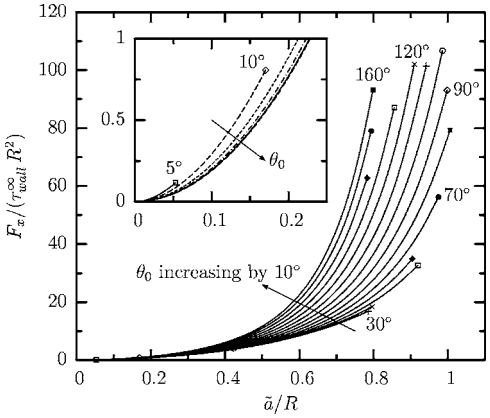

FIG. 15. The total force F_x exerted on the cell as a function of the cell size $\tilde{a}/R$ for spreading angles $\theta_0=5^\circ,10^\circ,20^\circ,\ldots,160^\circ$ (increments of 10°). The inset shows the same variation for small and moderate angles $\theta_0=5^\circ,10^\circ,20^\circ,30^\circ,40^\circ,50^\circ$. (Note that $\tau^{\infty}_{\text{wall}}$ is the undisturbed shear stress on the vessel wall far from the cell.)

Figure 14 shows the influence of the spreading angle θ_0 on the normal force for a typical cell size, $\tilde{a}/R=0.30$. As this figure reveals, by increasing the spreading angle θ_0 for a given cell size, the upstream and downstream change in the normal force increases monotonically due to the corresponding increase in the flow blocking depicted earlier in Fig. 6(b).

Having considered the (local) shear stress and normal force on the cell and its vicinity, we now investigate the total hemodynamic force exerted on the cell. Figure 15 shows that the total force F_x exerted on the cell along the flow direction (i.e., the x axis) increases with the cell size $\tilde{a}/R$ for any spreading angle as well as with the spreading angle θ_0 for moderate and large cell sizes. The increase is much more pronounced at large cell sizes and spreading angles (as the curves for $\theta_0 \geqslant 90^\circ$ indicate) due to the resulting higher blocking to the vessel flow. For small cell sizes, increasing the spreading angle from small values the total force F_x decreases up to $\theta_0 \approx 50^\circ$ as shown in the figure's inset; for higher values of θ_0 the total force increases with the spreading angle.

To investigate further the nature of the force exerted on the cell, we separate the hemodynamic force on the cell into its two components, i.e., the shear force F_x^{shear} and the normal force F_x^n. The relative magnitude of the two force components is shown in Fig. 16. For large vessels (i.e., small $\tilde{a}/R$) the shear force F_x^{shear} contributes more to the total force than the normal force F_x^n but the contribution of the normal force cannot be neglected especially at large spreading angles. For example, even for $\tilde{a}/R \to 0$ the normal force on an endothelial cell with $\theta_0=60^\circ$ is 30% of the shear force; for an adherent leukocyte with $\theta_0=160^\circ$, F_x^n is close to 57% of F_x^{shear}. As the vessel radius decreases (i.e., $\tilde{a}/R$ increases), the relative contribution of the normal force to the hemodynamic force increases and at large cell sizes $\tilde{a}/R$ becomes dominant. The increase of the relative contribution of the normal force with the cell size is much faster for large spreading angles. Observe that for $\theta_0=120^\circ$ and $\tilde{a}/R=0.9$, the normal force F_x^n is 4.6 times greater than the shear force F_x^{shear}.

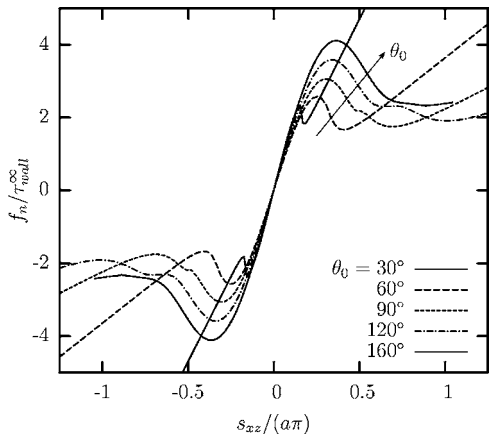

FIG. 14. Influence of the spreading angle θ_0 on the normal force: variation of the normal force f_n as a function of the arc length s_{xz} (measured from the cell peak) along the cross section of the geometry surface with the plane $y=0$ for a cell with $\tilde{a}/R=0.30$ and for $\theta_0=30^\circ,60^\circ,90^\circ,120^\circ,160^\circ$.

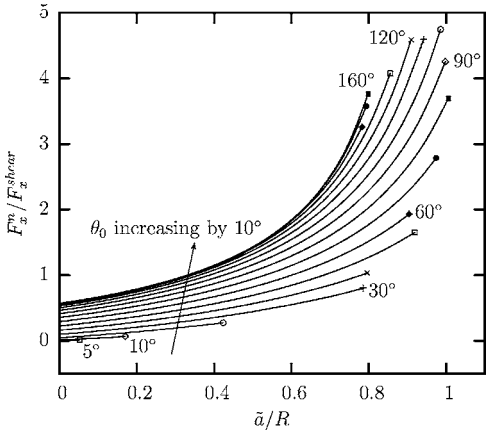

FIG. 16. Relative magnitude of the normal force F_x^n with respect to the shear force F_x^{shear} exerted on the cell as a function of the cell size $\tilde{a}/R$. The spreading angle θ_0 varies from 5° to 160°.

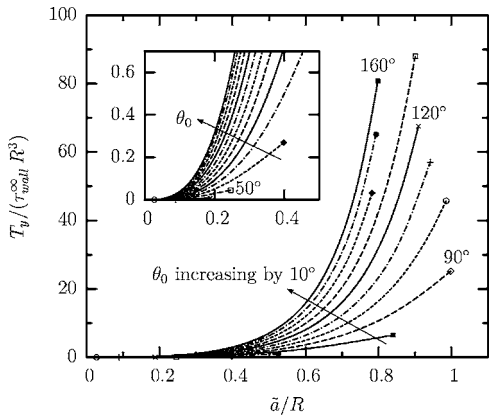

FIG. 17. The torque T_y exerted on the cell as a function of the cell size $\tilde{a}/R$ for spreading angles $\theta_0=5°, 10°, 20°, \ldots, 160°$ (increments of 10°). The inset shows the same variation for small values of the axes.

Figure 17 shows the torque T_y exerted on the cell as a function of the cell size $\tilde{a}/R$ for several spreading angles θ_0. We emphasize that T_y is defined with respect to the attachment center of the cell on the vessel wall [see Eq. (8) above]. This figure reveals that for a given angle θ_0, the torque exerted on the cell shows a monotonic increase with the cell size $\tilde{a}/R$; this increase is much more pronounced at large spreading angles. On the other hand, for a given cell size $\tilde{a}/R$, the torque on the cell increases with the spreading angle.

V. ANALYSIS

In our recent Letter on the normal force exerted on vascular endothelial cells,[23] we provided a scaling analysis for the shear and normal force acting on the endothelial cells that is formally valid for very small cell sizes $\tilde{a}/R$ and spreading angles θ_0. Here we present a short summary of this analysis since it helps to reveal the nature of the forces on the cell and explain their behavior with respect to the problem parameters, i.e., the cell size and the spreading angle. In the current study, our interest focuses on identifying (by employing our numerical results) the area of qualitative validity of the scaling analysis. As shown below, the physical predictions of the scaling analysis (and thus the associated physical understanding) are qualitatively valid for a wide range of vessels and spreading angles.

The shear force F_x^{shear} on the cell is proportional to the shear stress on the cell τ_c and the cell's surface area S_c. For small spreading angles θ_0 and small cell sizes $\tilde{a}/R$, the cell's surface area S_c is proportional to the contact region $A_c \sim \ell_x \ell_y$, where ℓ_x and ℓ_y are the length and the width of the cell, respectively, while for our problem $\ell_x \sim \ell_y$. Based on the cell's volume, we have $V \sim \tilde{a}^3 \sim \ell_x \ell_y \ell_z$, where the cell's height $\ell_z \sim \ell_x \tan\theta_0 \sim \ell_x \theta_0$ for small angles; thus $\ell_x \sim \ell_y \sim \tilde{a}\theta_0^{-1/3}$, $\ell_z \sim \tilde{a}\theta_0^{2/3}$, and $S_c \sim \tilde{a}^2 \theta_0^{-2/3}$. The shear stress τ_c on the cell is proportional to the undisturbed shear stress on the vessel wall far from the cell, $\tau^{\infty}_{\text{wall}}$. Thus for small angles and cell sizes, the shear force on the cell scales as

$$F_x^{\text{shear}} \sim \tau_c S_c \sim \tau^{\infty}_{\text{wall}} \tilde{a}^2 \theta_0^{-2/3}. \tag{9}$$

The normal force F_x^n on the cell may be divided into two distinct components. The first term F_x^{n1} arises from the undisturbed pressure gradient acting on the cell. For small spreading angles θ_0 and small cell sizes $\tilde{a}/R$, the pressure gradient in the flow direction scales as $\tau^{\infty}_{\text{wall}}/R$. The corresponding pressure change over the cell scales as $\Delta p^1 \sim \tau^{\infty}_{\text{wall}} \ell_x/R \sim \tau^{\infty}_{\text{wall}} (\tilde{a}/R)\theta_0^{1/3}$. The force component F_x^{n1} is proportional to Δp^1 and the frontal area of the cell, $A_f \sim \ell_y \ell_z \sim \tilde{a}^2 \theta_0^{1/3}$. Therefore, for small cell sizes and small spreading angles, the first normal force component scales as

$$F_x^{n1} \sim \Delta p^1 A_f \sim \tau^{\infty}_{\text{wall}} \frac{\tilde{a}^3}{R}, \tag{10}$$

i.e., it is independent of the spreading angle. The other component of the normal force F_x^{n0} arises from the disturbance of the base flow owing to the presence of the cell. Since the pressure change Δp^0 for this term in the absence of the cell is identically zero, in the presence of a cell Δp^0 scales as $\tau^{\infty}_{\text{wall}}\theta_0$ and thus the associated normal force scales as

$$F_x^{n0} \sim \Delta p^0 A_f \sim \tau^{\infty}_{\text{wall}} \tilde{a}^2 \theta_0^{4/3}. \tag{11}$$

The pressure gradient normal force component F_x^{n1} is negligible at small cell sizes due to its $\tilde{a}/R$ dependence but becomes the dominant component as the cell size increases. On the other hand, the base normal force component F_x^{n0} is negligible compared to F_x^{n1} at moderate and large cell sizes; however, for small cell sizes F_x^{n0} is the dominant component of the normal force F_x^n on the cell.

We emphasize again that the scaling analysis presented above is quantitatively valid for very small cell sizes and spreading angles. In particular, we have verified numerically its predictions for $\theta_0 = 1° - 5°$ and for $\tilde{a}/R \to 0$, i.e., the range of quantitative validity of the scaling analysis is extremely restricted. For a physical point of view, it is of great interest to see what is the range of qualitative validity of the scaling analysis and the associated physical understanding.

The scaling analysis predicts that the dependence of the shear force F_x^{shear} on $\tilde{a}/R$ and θ_0 is associated only with the corresponding dependence of the cell's surface area S_c since the shear stress on the cell τ_c is predicted to be independent of the two problem parameters. In particular, $S_c \sim \tilde{a}^2 \theta_0^{-2/3}$, i.e., it increases with the cell size but decreases with the spreading angle. Figure 18 shows that the scaling analysis predicts qualitatively the correct dependence of S_c on $\tilde{a}/R$ for all cases. In addition, it predicts the correct qualitative dependence of S_c on θ_0 for angles $\theta_0 \leqslant 80°$ and for small and moderate cell sizes $\tilde{a}/R$ as shown in the figure's inset. Note that for larger angles and for large cell sizes, the cell's surface area S_c increases with the spreading angle as shown in this figure; this behavior is not predicted by the scaling analysis.

Figure 19 shows the dependence of the shear stress $\tau_c \equiv F_x^{\text{shear}}/S_c$ over the cell on the problem parameters. For small and moderate cell sizes, τ_c is practically independent of the cell size for all angles, in qualitative agreement with the predictions of the scaling analysis. In the same range of cell sizes, the scaling analysis fails to predict the increase of τ_c with the spreading angle θ_0; however, this increase is

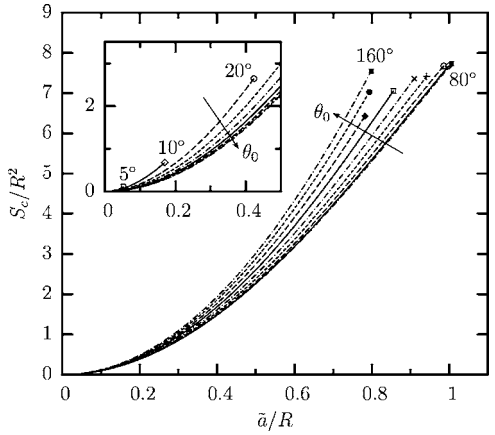

FIG. 18. The cell's surface area S_c as a function of the cell size $\tilde{a}/R$. The spreading angle θ_0 varies from 80° to 160° in increments of 10°. The inset shows the same variation for small and moderate angles 5°, 10°, 20°,…, 80° (increments of 10°).

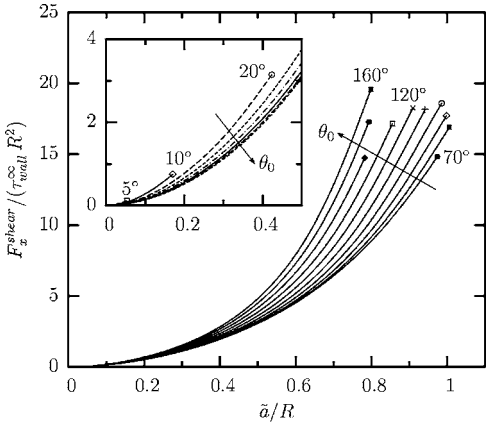

FIG. 20. The shear force F_x^{shear} exerted on the cell as a function of the cell size $\tilde{a}/R$. The spreading angle θ_0 varies from 70° to 160° in increments of 10°. The inset shows the same variation for small and moderate angles 5°, 10°, 20°,…, 70° (increments of 10°).

rather small even for the entire range of angles studied in this paper, $5° \leqslant \theta_0 \leqslant 160°$. For completeness, we note that the dependence of τ_c on the problem parameters is similar to that of the maximum shear stress magnitude $\tau^{\max}$ on the cell presented earlier in Fig. 11. (The magnitude of $\tau^{\max}$ is about four times greater than that of τ_c.)

For large cell sizes $\tilde{a}/R$, Figs. 18 and 19 show that while both surface area S_c and shear stress τ_c increase with the cell size, the former shows a faster increase and thus it contributes more to the total shear force F_x^{shear} on the cell. This conclusion is also in qualitative agreement with the predictions of the scaling analysis. Therefore, the predictions of the scaling analysis for the shear force F_x^{shear} on the cell are qualitatively valid for a much wider range of the parameter space than its formal range of validity. This is also shown in Fig. 20, where we plot the variation of F_x^{shear} with respect to the cell size $\tilde{a}/R$ and the spreading angle θ_0.

The scaling analysis predicts that the normal force F_x^n on the cell is affected by the dependence of both the pressure change Δp^0 over the cell and of the cell's frontal area A_f on the problem parameters. In particular, the cell's frontal area is predicted to scale as $A_f \sim \tilde{a}^2 \theta_0^{1/3}$, i.e., it increases with both the cell size and the spreading angle due to the corresponding increase of the cell's height, ℓ_z. As shown in Fig. 21, where we plot the frontal area of the cell A_f as a function of the cell size and the spreading angle, the scaling analysis predicts the correct qualitative dependence for the entire range of the parameter space.

Figure 22 shows the pressure change $\Delta p \equiv F_x^n/A_f$ over the cell as a function of the cell size and the spreading angle. Note that Δp increases with both parameters; the increase is more dramatic at large cell sizes and spreading angles due to the associated pressure gradient increase resulting from the higher flow blocking. For small cell sizes, where the normal force is dominated by its base component F_x^{n0}, the scaling analysis predicts that $\Delta p \equiv \Delta p^0 \sim \tau_{\text{wall}}^{\infty} \theta_0$, i.e., it increases with the spreading angle while it is independent of the cell size $\tilde{a}/R$. Therefore, the scaling analysis fails to predict the increase of the pressure change with the cell size. However, its prediction of the dependence on θ_0 is in qualitative agreement with our numerical results. We emphasize that Δp does not go to zero as $\tilde{a}/R \to 0$ for finite spreading angles $\theta_0 > 0$ as shown in the figure's inset, in agreement with the predictions of the scaling analysis, $\Delta p^0 \sim \tau_{\text{wall}}^{\infty} \theta_0$.

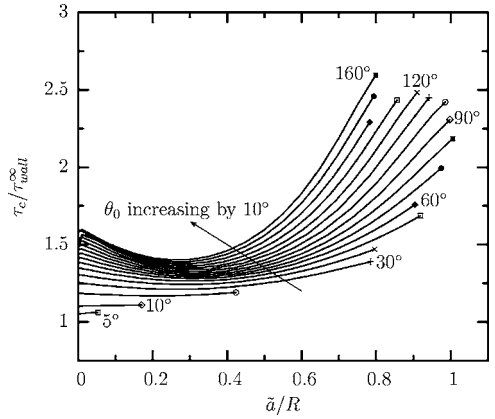

FIG. 19. The shear stress on the cell $\tau_c \equiv F_x^{\text{shear}}/S_c$ as a function of the cell size $\tilde{a}/R$. The spreading angle θ_0 varies from 5° to 160°.

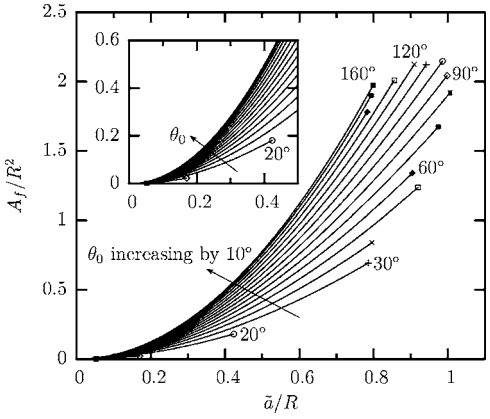

FIG. 21. The frontal area of the cell A_f as a function of the cell size $\tilde{a}/R$. The spreading angle θ_0 varies from 5° to 160°. The inset shows the same variation for small cell sizes $\tilde{a}/R$.

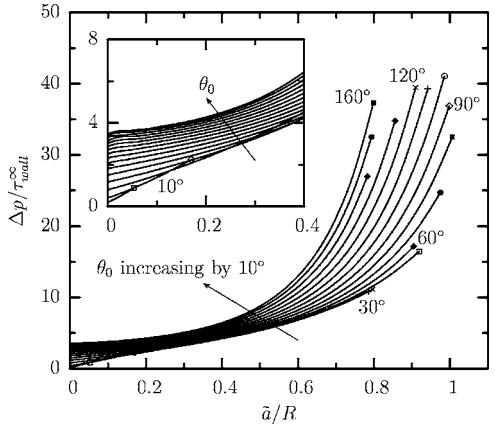

FIG. 22. The pressure change $\Delta p \equiv F_x^n/A_f$ as a function of the cell size $\tilde{a}/R$. The spreading angle θ_0 varies from 5° to 160°. The inset shows the same variation for small cell sizes $\tilde{a}/R$.

From our analysis above as well as our numerical results for the cell's frontal area A_f and the pressure change Δp presented in Figs. 21 and 22, respectively, it is now obvious that the normal force $F_x^n \sim \Delta p A_f$ increases monotonically with both the cell size $\tilde{a}/R$ and the spreading angle θ_0; the increase is much more pronounced at high cell sizes and spreading angles, as shown in Fig. 23. Comparing Figs. 21 and 22, we note that the rapid increase of F_x^n at large cell sizes and spreading angles results mostly from the corresponding increase of the pressure change Δp over the cell, i.e., the pressure gradient.

VI. DISCUSSION

In this paper, we have conducted an extensive study on the hemodynamic forces exerted on vascular endothelial cells or leukocytes adhering to the surface of blood vessels. By taking into consideration the curvature of the vessel (which has been modeled as a cylindrical tube) and varying the cell-to-vessel size, our results are applicable to the entire range of vessels including capillaries (with a typical diameter of 8 μm), arterioles, and venules (with a typical diameter of 10–140 μm) as well as arteries and veins (with a typical diameter up to a few mm).[25] We have also considered a wide range of cell spreading, from much spread cells with a spreading angle $\theta_0 = 5°$ to less spread cells with $\theta_0 = 160°$.

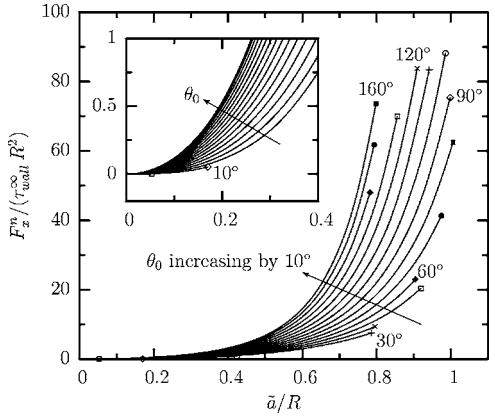

FIG. 23. The normal force F_x^n exerted on the cell as a function of the cell size $\tilde{a}/R$. The spreading angle θ_0 varies from 5° to 160°. The inset shows the same variation for small cell sizes $\tilde{a}/R$.

A cell adhering to the surface of a blood vessel causes a significant amplification to the shear stress distribution over the cell and its vicinity. For a given spreading angle θ_0, the shear stress amplification is a weak function of the cell size $\tilde{a}/R$ for small and moderate cell sizes as clearly shown in Figs. 8, 9, and 11. However, for large cell sizes (or small vessels for a given cell), the shear stress amplification increases rapidly with the cell size, as shown in Fig. 11. On the other hand, the shear stress distribution over the cell depends strongly on the spreading angle θ_0 at all cell sizes, as shown in Figs. 10 and 11. The comprehensive figure 11 clearly reveals that large spreading angles θ_0 are accompanied with a very fast increase in the shear stress for large cell sizes $\tilde{a}/R$ (or small vessels for a given cell). Thus, endothelial cells and especially adherent leukocytes cause a significant amplification to the shear stress distribution in all vessels, especially in capillaries and post-capillaries. The presence of endothelial cells and adherent leukocytes causes a significant amplification to the normal force (or pressure) distribution over the cell and its vicinity as well. This amplification is a monotonic function of both the cell size and the spreading angle, as shown in Figs. 13 and 14.

The (total) hemodynamic force F_x on the cell increases with the cell size $\tilde{a}/R$ for any spreading angle θ_0 as well as with the spreading angle θ_0 for moderate and large cell sizes, as shown in Fig. 15. For small cell sizes, increasing the spreading angle from small values, the total force F_x decreases up to $\theta_0 \approx 50°$ as shown in the figure's inset; for higher values of θ_0 the total force increases with the spreading angle. Thus, the dependence of F_x on the spreading angle is rather complicated.

To clarify the physical origin of the hemodynamic forces on the cells, we separated the total force F_x into its two components, i.e., the shear force F_x^{shear} and the normal force F_x^n. Our analysis presented in Sec. V helps us to understand the nature of the hemodynamic force F_x on the cell and its dependence on the problem parameters. This analysis is based on our numerical results for relevant geometric variables (i.e., the cell's surface area S_c and frontal area A_f) and physical quantities (i.e., the shear stress τ_c and pressure change Δp over the cell). At small cell sizes, the decrease of F_x with increasing spreading angle for small and moderate angles θ_0 (shown in the inset of Fig. 15) is caused by the dominant shear component F_x^{shear} and thus by the associated decrease of the cell's surface area S_c shown in Fig. 18. The rapid increase of F_x at large cell sizes and spreading angles shown in Fig. 15 results mainly from the normal force F_x^n exerted on the cell and thus by the associated increase of the cell's frontal area A_f (seen in Fig. 21) and especially that of the pressure change Δp over the cell due to pressure gradient shown in Fig. 22.

In Sec. V, we also compared our numerical results with the predictions of the scaling analysis for very large vessels and very spread cells (which is thus extremely restricted quantitatively to $\theta_0 \ll 1$ and $\tilde{a}/R \ll 1$). Our analysis shows that the predictions and the associated physical understand-

ing of the scaling analysis are qualitatively valid for a wide range of vessels and spreading angles.

Our study shows that the normal force contributes significantly both to the (local) force distribution over the cell and its vicinity as well as to the (total) hemodynamic force on the cell. The contribution of the normal force cannot be neglected for all cell sizes $\tilde{a}/R$ especially for less spread cells, as shown in Fig. 16. We have also identified the nature of the normal force on the cell. In particular, for large vessels the normal force is dominated by its base pressure component F_x^{n0}, which contributes significantly to the hemodynamic force especially for less spread cells (e.g., adherent leukocytes) as shown clearly in Fig. 16. For moderate and small vessels, the pressure gradient normal force F_x^{n1} contributes significantly to the hemodynamic force on the cell and even becomes the dominant component at small vessels (see Fig. 16) due to the associated high flow blocking. In all cases, we also expect that flowing blood particles (such as red and white cells) should increase the normal force contribution to the hemodynamic force on the endothelial cells and adherent leukocytes due to the associated higher flow blocking they induce. Since the endothelial cells convert the forces on them into biochemical signals, we expect the behavior of these cells to be strongly affected by the normal force exerted on them. The same conclusion is also true for adherent leukocytes, where the effects of the normal force are stronger due to the larger spreading angles.

Our study also shows that the spreading of the cell on the vessel surface cannot be discounted, especially at small vessels. For example, Figs. 15, 20, and 23 clearly show a great amplification of the hemodynamic force and its two components (i.e., shear and normal force) for less spread cells. This conclusion is in direct contrast to the behavior in arteries and veins, where the cell spreading has limited effects on the shear stress amplification caused by the presence of the cell.[37] Therefore, results from arteries and veins should not be used to explain the physical behavior in smaller vessels. Our study also suggests that, in regions of high hemodynamic forcing, endothelial cells and adherent leukocytes may be more spread out on the vessel surface to minimize the forces on them.

ACKNOWLEDGMENTS

This work was supported in part by the National Science Foundation. Acknowledgment is made to the Donors of the American Chemical Society Petroleum Research Fund for partial support of this research. Some computations were performed on the multiprocessor supercomputer IBM pSeries 690 provided by the National Center for Supercomputing Applications (NCSA) in Illinois.

[1] J. A. Frangos, S. G. Eskin, L. V. McIntire, and C. L. Ives, "Flow effects on prostacyclin production by cultured human-endothelial cells," Science **227**, 1477 (1985).
[2] J. A. Frangos, T. Y. Huang, and C. B. Clark, "Steady shear and step changes in shear stimulate endothelium via independent mechanisms—Superposition of transient and sustained nitric oxide production," Biochem. Biophys. Res. Commun. **224**, 660 (1996).
[3] H. W. Sill, Y. S. Chang, J. R. Artman, J. A. Frangos, T. M. Hollis, and J. M. Tarbell, "Shear stress increases hydraulic conductivity of cultured endothelial monolayers," Am. J. Physiol. Heart Circ. Physiol. **268**, H535 (1995).
[4] L. Demaio, Y. S. Chang, T. W. Gardner, J. M. Tarbell, and D. A. Antonetti, "Shear stress regulates occludin content and phosphorylation," Am. J. Physiol. Heart Circ. Physiol. **281**, H105 (2001).
[5] S. Sheikh, G. E. Rainger, Z. Gale, M. Rahman, and G. B. Nash, "Exposure to fluid shear stress modulates the ability of endothelial cells to recruit neutrophils in response to tumor necrosis factor-*a*: A basis for local variations in vascular sensitivity to inflammation," Blood **102**, 2828 (2003).
[6] T. K. Hsiai, S. K. Cho, P. K. Wong, M. Ing, A. Salazar, A. Sevanian, M. Navab, L. L. Demer, and C. M. Ho, "Monocyte recruitment to endothelial cells in response to oscillatory shear stress," FASEB J. **17**, 1648 (2003).
[7] S. Weinbaum, X. Zhang, Y. Han, H. Vink, and S. C. Cowin, "Mechanotransduction and flow across the endothelial glycocalyx," Proc. Natl. Acad. Sci. U.S.A. **100**, 7988 (2003).
[8] N. Resnick, H. Yahav, and A. Shay-Salit, "Fluid shear stress and the vascular endothelium: For better and for worse," Prog. Biophys. Mol. Biol. **81**, 177 (2003).
[9] B. P. Helmke, R. D. Goldman, and P. F. Davies, "Rapid displacement of vimentin intermediate filaments in living endothelial cells exposed to flow," Circ. Res. **86**, 745 (2000).
[10] D. P. Gaver and S. Kute, "A theoretical model study of the influence of fluid stresses on a cell adhering to a microchannel wall," Biophys. J. **75**, 721 (1998).
[11] S. R. Hodges and O. E. Jensen, "Spreading and peeling dynamics in a model of cell adhesion," J. Fluid Mech. **460**, 381 (2002).
[12] G. B. Chapman and G. R. Cokelet, "Model studies of leukocyte-endothelium-blood interactions. II. Hemodynamic impact of leukocytes adherent to the wall of post-capillary vessels," Biorheology **34**, 37 (1997).
[13] A. L. Hazel and T. J. Pedley, "Vascular endothelial cells minimize the total force on their nuclei," Biophys. J. **78**, 47 (2000).
[14] G. B. Chapman and G. R. Cokelet, "Model studies of leukocyte-endothelium-blood interactions. I. The fluid flow drag force on the adherent leukocyte," Biorheology **33**, 119 (1996).
[15] G. B. Chapman and G. R. Cokelet, "Flow resistance and drag forces due to multiple adherent leukocytes in postcapillary vessels," Biophys. J. **74**, 3292 (1998).
[16] M. Sugihara-Seki and R. Skalak, "Force acting on spheres adhered to a vessel wall," Biorheology **34**, 249 (1997).
[17] M. Sugihara-Seki, "Flow around cells adhered to a microvessel wall. I. Fluid stresses and forces acting on the cells," Biorheology **37**, 341 (2000).
[18] M. Sugihara-Seki, "Flow around cells adhered to a microvessel wall. II: Comparison to flow around adherent cells in channel flow," Biorheology **38**, 3 (2001).
[19] M. Sugihara-Seki and G. W. Schmid-Schönbein, "The fluid shear stress distribution on the membrane of leukocytes in the microcirculation," J. Biomech. Eng. **125**, 628 (2003).
[20] B. Das, P. C. Johnson, and A. S. Popel, "Computational fluid dynamic studies of leukocyte adhesion effects on non-Newtonian blood flow through microvessels," Biorheology **37**, 239 (2000).
[21] X. H. Liu and X. Wang, "The deformation of an adherent leukocyte under steady shear flow: A numerical study," J. Biomech. **37**, 1079 (2004).
[22] N. A. N'Dri, W. Shyy, and R. Tran-Soy-Tay, "Computational modeling of cell adhesion and movement using a continuum-kinetics approach," Biophys. J. **85**, 2273 (2003).
[23] Y. Wang and P. Dimitrakopoulos, "Normal force exerted on vascular endothelial cells," Phys. Rev. Lett. **96**, 028106 (2006).
[24] M. R. King, "Biomedical applications of microchannel flows," in *Heat Transfer and Fluid Flow in Minichannels and Microchannels*, edited by S. G. Kandlikar, S. Garimella, D. Li, S. Colin, and M. R. King (Elsevier, New York, 2006).
[25] S. A. Berger, W. Goldsmith, and E. R. Lewis, *Introduction to Bioengineering* (Oxford University Press, Oxford, 1996).
[26] A. S. Popel and P. C. Johnson, "Microcirculation and hemorheology," Annu. Rev. Fluid Mech. **37**, 43 (2005).
[27] M. F. Coughlin and G. W. Schmid-Schönbein, "Pseudopod projection and cell spreading of passive leukocytes in response to fluid shear stress," Biophys. J. **87**, 2035 (2004).
[28] C. Migliorini, Y. H. Qian, H. D. Chen, E. B. Brown, R. K. Jain, and L. L. Munn, "Red blood cells augment leukocyte rolling in a virtual blood vessel," Biophys. J. **83**, 1834 (2002).
[29] C. Pozrikidis, *Boundary Integral and Singularity Methods for Linearized Viscous Flow* (Cambridge University Press, Cambridge, 1992).

[30]G. P. Muldowney and J. J. L. Higdon, "A spectral boundary element approach to three-dimensional Stokes flow," J. Fluid Mech. **298**, 167 (1995).
[31]P. Dimitrakopoulos and J. J. L. Higdon, "On the displacement of three-dimensional fluid droplets from solid surface in low-Reynolds-number shear flows," J. Fluid Mech. **377**, 189 (1998).
[32]C. Canuto, M. Y. Hussaini, A. Quarteroni, and T. A. Zang, *Spectral Methods in Fluid Dynamics* (Springer, New York, 1988).
[33]J. J. L. Higdon, "Stokes flow in arbitrary two-dimensional domains: Shear flow over ridges and cavities," J. Fluid Mech. **159**, 195 (1985).
[34]C. Pozrikidis, "Shear flow over a protuberance on a plane wall," J. Eng. Math. **31**, 29 (1997).
[35]C. Pozrikidis, "Effect of pressure gradient on viscous shear flow past an axisymmetric depression or protuberance on a plane wall," Comput. Fluids **29**, 617 (2000).
[36]M. Tobak and D. J. Peake, "Topology of three-dimensional separated flows," Annu. Rev. Fluid Mech. **14**, 61 (1982).
[37]L. A. Olivier and G. A. Truskey, "A numerical analysis of forces exerted by laminar flow on spreading cells in a parallel plate flow chamber assay," Biotechnol. Bioeng. **42**, 963 (1993).